Polarization dynamics of the fundamental vector soliton of isotropic Kerr media

Michaël Delqué,* Gil Fanjoux, and Thibaut Sylvestre
Département d'Optique P.M. Duffieux, Institut FEMTO-ST, Université de Franche-Comté, CNRS UMR 6174, F-25030 Besançon, France
(Received 21 July 2006; revised manuscript received 17 October 2006; published 22 January 2007)

We characterize fully the polarization dynamics of the fundamental vector soliton of isotropic Kerr materials by measuring the Stokes parameters of an elliptically polarized self-trapped optical beam propagating in a slab planar waveguide. Our experiment clearly shows that this two-component spatial vector soliton exhibits both the so-called ellipse rotation and curved-shape ellipticity that are due to the self-induced nonlinear birefringence between the two components of the vector soliton. The polarization of the vector soliton is accurately determined both in the transverse and longitudinal directions and comparisons with numerical simulations based on two coupled nonlinear Schrödinger equations provide an excellent quantitative agreement. Spatiotemporal numerical simulations that take into account the finite pulse duration of the experimental input optical beam must, however, be used to match rigorously the measured state of polarization of the vector soliton.

DOI: 10.1103/PhysRevE.75.016611 PACS number(s): 42.65.Tg, 42.65.Jx

I. INTRODUCTION

Since the pioneering experimental work of Maker *et al.* in 1964 [1], the dynamical evolution of the polarization state of light in nonlinear media has been the subject of extensive basic and applied research. This has led to the discovery of new nonlinear phenomena such as polarization bound states and vector solitary waves [2–4]. New instability regimes were also found such as polarization, modulation, or symmetry-breaking instabilities [5–12]. Most of these nonlinear polarization dynamics have been theoretically modeled by a set of coupled nonlinear Schrödinger equations (CNLSE). These equations were first investigated for birefringent nonlinear media in the (1+1)D propagation geometry. In that case, stationary solutions have been demonstrated to exist in the form of polarization bound states counterbalancing the linear birefringence, and leading to the so-called vector soliton [3,4]. Polarization and modulation instabilities were also reported in the small and high birefringence regime of optical waveguides [5,8,11,13–21]. For instance, the domain of existence of modulation instability and, consequently, of vector solitons is extended in the normal dispersion regime of birefringent optical fibers because of cross-phase modulation [6,7,10,19,22]. Other studies have focused on stationary [23,24] or periodically evolving solutions [25–27]. We must note that most theoretical and experimental investigations have been performed in birefringent media in contrast with Maker *et al.*'s [1] initial work which was concerned with isotropic materials and for which very few studies have been conducted [28,29]. Interestingly, however, in addition to the well-known linearly and circularly polarized solitons, isotropic media also support elliptically polarized fundamental vector solitons (EPVS) [30]. This stationary solution exists because of the incoherent coupling between its two circularly polarized components in a way akin to the Manakov vector soliton which was experimentally reported in a birefringent AlGaAs planar waveguide in 1996 [31]. The EPVS differs, however, in several respects from the Manakov soliton. As mentioned in Ref. [31], the Manakov soliton exists even in the presence of linear birefringence because the incoherent coupling between its two linearly polarized components is due to the requirement that the strength of self-phase modulation equals that of cross-phase modulation. On the contrary, the EPVS exists for arbitrary cross-phase modulation strength but only in nonbirefringent media. Moreover, in a well-chosen rotating frame, the Manakov soliton can be described by a single evolution equation while there exists no such reference frame for the EPVS of isotropic media. In Ref. [32] we reported the first observation of a fundamental elliptically polarized vector soliton. This vector soliton was observed in the spatial domain in a Kerr carbon disulfide (CS_2) liquid slab planar waveguide but only partial experimental evidence was reported, namely the curved ellipticity factor and the polarization rotation. In the current work, we provide a full experimental characterization of the polarization dynamics of the EPVS by measuring input and output Stokes parameters in the transverse direction. With this technique, we are able to measure the complete evolution of the polarization state on the Poincaré sphere. In addition to the so-called ellipse rotation, we clearly show that the EPVS exhibits a nonuniform ellipticity profile, as predicted theoretically [30]. The polarization rotation and ellipticity curvature of the vector soliton are accurately measured and compared with numerical simulations of the two coupled nonlinear Schrödinger equations. In particular, we show that the finite pulse duration of the experimental input optical beam must be carefully taken into account as it has a strong impact on the transverse polarization of the vector soliton, mainly because the pulse wings experience less self-focusing and more diffraction than the peak of the pulse. As a result, the polarization state dynamics of the vector soliton is more complex than for the case of a pure continuous-wave field. We then present spatiotemporal numerical simulations that are consistent with this explanation and that are in excellent agreement with polarization measurements. This paper is organized as follows. In Sec. II, we present the theory of vector nonlinear propagation in isotropic conditions and the polarization representation. Numerical simulations of the vector soliton and its unique po-

*Electronic address: michael.delque@univ-fcomte.fr

larization dynamics are investigated numerically in Sec. III. Section IV is devoted to the experimental evidence of the vector soliton and its complete polarization characterization. Finally, in Sec. V we draw our conclusions.

II. THEORY

A. Nonlinear Schrödinger equations

Scalar propagation in a single-mode planar Kerr waveguide is modeled by the usual (1+1)D nonlinear Schrödinger (NLS) equation which governs the propagation of linearly polarized solitons in the steady-state regime. For vector nonlinear propagation, similar NLS equations are used for each polarization component with additional coupling terms. Assuming a lossless and dispersionless nonlinear medium, the polarization evolution along the waveguide (z direction) can be modeled by two coupled NLS equations that read [33]

$$\frac{\partial E_x}{\partial z} = \frac{i}{2k_x}\frac{\partial^2 E_x}{\partial x^2} + i\gamma\{[|E_x|^2 + (1-B)|E_y|^2]E_x + BE_y^2E_x^\star \exp(2i\Delta kz)\},$$

$$\frac{\partial E_y}{\partial z} = \frac{i}{2k_y}\frac{\partial^2 E_y}{\partial x^2} + i\gamma\{[|E_y|^2 + (1-B)|E_x|^2]E_y + BE_x^2E_y^\star \exp(-2i\Delta kz)\}, \quad (1)$$

where x is the spatial coordinate along the unguided transverse direction of the waveguide. E_x, E_y are the transverse electric (TE) and transverse magnetic (TM) orthogonal linearly polarized components of the electric field, respectively, while k_x and k_y are the wave vectors, and $\Delta k = k_y - k_x$ is the group-velocity mismatch due to the intrinsic linear birefringence. $\gamma = 2\pi n_2/\lambda_0$ is the nonlinear coefficient with $n_2 = 3.5 \times 10^{-18}$ m^2 W^{-1} (see, e.g., Ref. [34]) the nonlinear refractive index in CS_2 and λ_0 the wavelength in vacuum. $B = \chi_{xyyx}/\chi_{xxxx}$ represents the polarization susceptibility ratio. As the Kerr nonlinearity of CS_2 mainly relies on the molecular reorientation effect in the subnanosecond regime, $B = 3/4$ [35]. Terms on the right-hand side of Eqs. (2) stand for diffraction, self-phase modulation (SPM), cross-phase modulation (XPM), and four-wave mixing (FWM), respectively. FWM is a coherent coupling process which can lead to strong energy exchange between E_x and E_y depending on the magnitude of Δk. In isotropic or low-birefringence media for which $\Delta k \simeq 0$, the energy transfer can be very efficient, thus leading to nonlinear effects such as polarization instability, whereas in highly birefringent media, no energy exchange occurs efficiently.

In isotropic media, $k_x = k_y = k$ and Eqs. (2) can be rewritten in a more convenient way in the basis of circular polarizations:

$$\frac{\partial U}{\partial z} = \frac{i}{2k}\frac{\partial^2 U}{\partial x^2} + i\gamma[(1-B)|U|^2 + (1+B)|V|^2]U,$$

$$\frac{\partial V}{\partial z} = \frac{i}{2k}\frac{\partial^2 V}{\partial x^2} + i\gamma[(1-B)|V|^2 + (1+B)|U|^2]V, \quad (2)$$

where $U, V = (E_x \pm iE_y)/\sqrt{2}$ are the right-handed and the left-handed circularly polarized components of the electric field, respectively. In this basis the field components in Eqs. (2) are incoherently coupled, i.e., no energy exchange can occur between U and V. With $B = 3/4$, Eqs. (2) show that we can expect strong nonlinear circular birefringence as XPM is seven times stronger than SPM, resulting in significant polarization rotation.

B. Polarization dynamics

As mentioned before, an isotropic medium is a necessary condition for the experimental observation of the fundamental EPVS. Nonetheless, it is interesting to understand first the mutual influence of linear and nonlinear birefringence of the guiding structure on the nonlinear polarization dynamics. This evolution along the propagation direction is modeled by Eqs. (2) and can be examined with the following Stokes parameters [36]:

$$s_0(x,z) = |E_x|^2 + |E_y|^2 = [s_1(x,z)^2 + s_2(x,z)^2 + s_3(x,z)^2]^{1/2},$$

$$s_1(x,z) = |E_x|^2 - |E_y|^2,$$

$$s_2(x,z) = 2\,\mathrm{Re}(E_xE_y^\star),$$

$$s_3(x,z) = 2\,\mathrm{Im}(E_xE_y^\star), \quad (3)$$

which describe the spatially resolved polarization state of the field across the beam in the transverse direction (x) for various positions (z) along the waveguide. In terms of circularly polarized components, the Stokes parameters can be rewritten as

$$s_0(x,z) = |U|^2 + |V|^2,$$

$$s_1(x,z) = 2\,\mathrm{Re}(UV^\star),$$

$$s_2(x,z) = 2\,\mathrm{Im}(UV^\star),$$

$$s_3(x,z) = |U|^2 - |V|^2. \quad (4)$$

We also define the Stokes parameter's integral equation, as in Ref. [27]:

$$S_{0,1,2,3}(z) = \int_{-\infty}^{+\infty} s_{0,1,2,3}(x,z)dx, \quad (5)$$

which is a measure of the global polarization state of the beam at various positions along the waveguide. Of course, these integrated Stokes parameters imply a loss of coherence when the polarization is not constant along the integrated transverse direction. This means that the beam can appear as being partially polarized with $S_1^2 + S_2^2 + S_3^2 < S_0^2$ which is one of the interests of using integrated Stokes parameters, as we will see below. Figure 1 shows the equivalence between the two common polarization representations (polarization el-

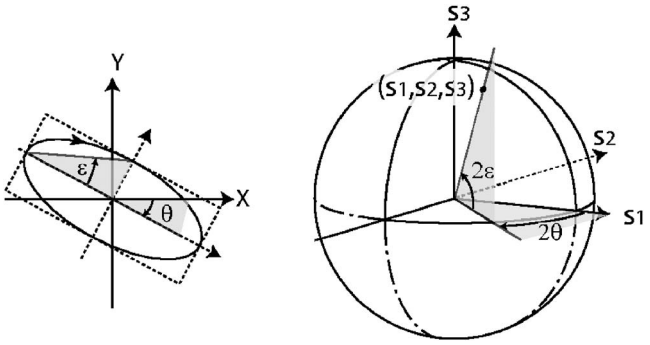

FIG. 1. Commonly used polarization representations: polarization ellipse and Stokes parameters on the Poincaré sphere.

lipse and Stokes parameters on the Poincaré sphere). The θ and ε parameters correspond to the orientation of the polarization ellipse and to the ellipticity angle, respectively, and read as

$$\theta(x,z) = \frac{1}{2}\arctan\left[\frac{s_2(x,z)}{s_1(x,z)}\right], \tag{6a}$$

$$\varepsilon(x,z) = \frac{1}{2}\arcsin\left[\frac{s_3(x,z)}{s_0(x,z)}\right]. \tag{6b}$$

We also define the normalized ellipticity factor as

$$q(x,z) = \frac{|U|^2 - |V|^2}{|U|^2 + |V|^2} = \frac{s_3(x,z)}{s_0(x,z)} = \sin(2\varepsilon), \tag{7}$$

$q=0$ corresponds to linear polarization while $q=\pm 1$ is associated with right-handed and left-handed circular polarization, respectively.

Figure 2(a)–2(d) illustrate some polarization trajectories on the Poincaré sphere obtained from numerical integration of Eqs. (2) for different values of linear birefringence. These trajectories represent the global polarization evolution of a light beam during the propagation over a long distance of $7L_D$ where $L_D = 2.27\omega^2 n_o/\lambda$ stands for the diffraction length. ω is the full width at half maximum (FWHM) of the beam while n_o is the linear refractive index of the material (the factor of 2.27 in the definition of L_D arises from the use of the FWHM rather than the $1/e$ full width). We chose such a long propagation distance to make the different polarization behaviors clearly recognizable. In the absence of nonlinearity, Fig. 2(a) shows that the polarization trajectory evolves in a plane perpendicular to the S_1 axis. The polarization state regularly rotates around the S_1 axis independently of the initial polarization state. The invariance of the S_1 parameter with z is directly related to the absence of energy exchange between E_x and E_y [see Eqs. (3)]. When nonlinearity enters into play, various trajectories can be observed. For instance, in nonbirefringent media, Fig. 2(b) shows that the polarization evolves in a plane perpendicular to the S_3 axis, and that the polarization state regularly rotates around the S_3 axis independently of the initial polarization state. In this case, the invariance of the integrated Stokes parameter $S_3(z)$ results from the absence of energy exchange between U and V during propagation [see Eqs. (4)]. Therefore the nonlinearly induced birefringence leads to the rotation of the polarization ellipse, i.e., to the variation of the θ parameter. Note that the conservation of $S_3(z)$ does not rule out variation of the nonintegrated Stokes parameter $s_3(x,z)$ along the transverse dimension due to the ellipticity variation, as we will see thereafter. When linear and nonlinear birefringence are present simultaneously, the polarization trajectories exhibit a more complex behavior [see Fig. 2(c)]. On the one hand, none of the integrated Stokes parameters remain constant during the propagation. On the other hand, polarization trajectories strongly depend on the initial polarization state, as shown in Fig. 2(c) where two trajectories with different starting points are plotted in solid and dotted lines. More details about this case can be found in Refs. [26,27,37]. Finally, when linear birefringence is at least one order of magnitude smaller than nonlinear birefringence [Fig. 2(d)], the polarization trajectories are close to that of Fig. 2(b). As long as the propagation distance remains small, the influence of the initial condition is strongly reduced compared to the previous case. As a result, the $S_3(z)$ parameter is roughly constant and the medium behaves like an isotropic one.

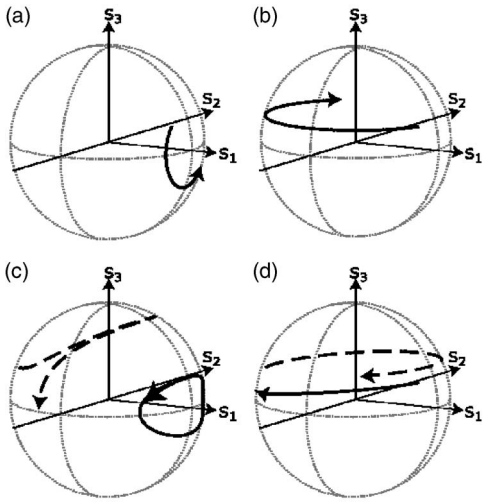

FIG. 2. Typical polarization evolution for $7L_D$ propagation of the integrated Stokes parameters on the Poincaré sphere. (a) Linear evolution in birefringent media (beat length of $L=11L_D$), (b) nonlinear evolution in isotropic media, (c) nonlinear evolution in birefringent media (beat length of $L=11L_D$): two examples in solid and dotted lines for two different starting points, and (d) nonlinear evolution in quasi-isotropic media (beat length of $L=110L_D$): idem.

III. NUMERICAL SIMULATIONS

From a numerical point of view, the input field can be described easily in the spatial domain by assuming a constant continuous-wave field in the time domain. However, in most spatial soliton experiments, high-power short pulsed laser beams have been used so far, thus resulting in the diffraction of the pulse wings. In the same way, we can expect a strong influence of the finite pulse duration on the polarization dynamics of a spatial EPVS, as the pulse wings will experience different polarization rotation than the pulse center. This is the reason we will take into account in following the finite

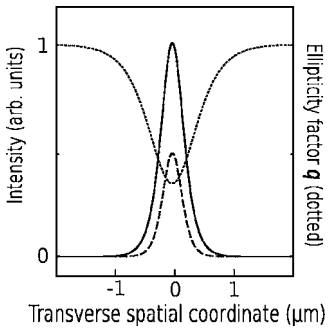

FIG. 3. The elliptically polarized fundamental vector soliton envelopes $U(x)$ (solid line) and $V(x)$ (dashed lines), and the corresponding ellipticity distribution $q(x)$ (dotted line).

pulse duration of the input field. As we will see, the comparison between both input conditions (cw or pulsed) will allow us to well interpret the experimental polarization measurements.

A. Spatial profiles

1. Exact solution

Figure 3 shows the exact EPVS solution of Eqs. (2) in an isotropic medium [30]. As can be seen, the transverse profiles of the U and V components have a hyperbolic-secant shape, and the polarization ellipticity factor is nonuniform across the beam and exhibits a dip at the center (dotted line) that depends on the U/V input ratio [30]. As the EPVS is the exact and stable solution, these transverse profiles do not change during propagation, i.e., are independent of z. The instantaneous Stokes parameters of the field do, however, vary along the beam. To get a better insight into the longitudinal evolution of the transverse polarization profile, the polarization dynamics of the EPVS is plotted on the Poincaré sphere in Fig. 4. Each arc of a circle on the sphere corresponds to the Stokes parameters of the soliton in the transverse dimension x at a fixed distance z. More precisely, the length of each arc Δx corresponds to twice the FWHM of the beam. The total propagation distance z_{max} corresponds to $7L_D$, whereas the propagation distance Δz between two arcs is equal to $z_{max}/20$. For each segment, the bottom point (lowest value of s_3) corresponds to the peak of the soliton and the top point (highest value of s_3) corresponds to the wings at one FWHM distance of the maximum. This particular representation is very useful because one arc of a circle in Fig. 4 reveals the transverse polarization variation only due to ellipticity curvature [Eq. (6b)], while the length of the arc represents the maximum ellipticity variation at the beam center.

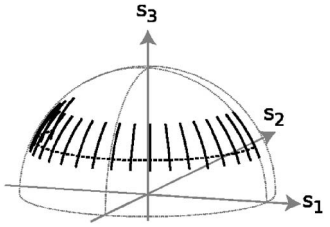

FIG. 4. Poincaré sphere representation of the evolution of the Stokes parameters of an exact EPVS over a propagation distance of $7L_D$. The dashed line represents the integrated Stokes parameter evolution.

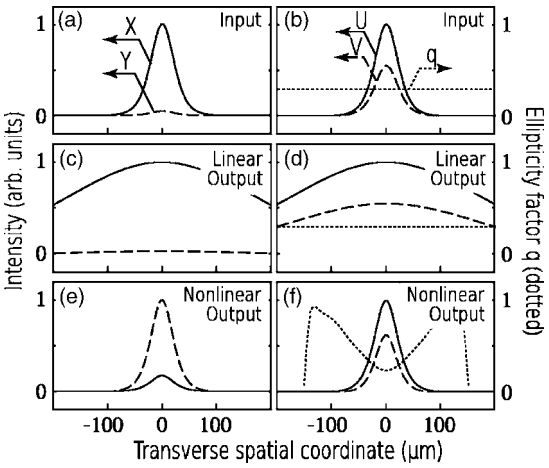

FIG. 5. Theoretical results: (a), (c), and (e): E_x (solid line) and E_y (dashed line) intensity profiles for, respectively, the input beam (FWHM=49 μm), the output beam at low power (FWHM >400 μm), and the output beam in soliton regime (FWHM =49 μm). (b), (d), and (f): corresponding U (solid line), V (dashed line), and q (dotted line) profiles. Note that in the soliton regime, FWHM(U)=53 μm is different from FWHM(V)=49 μm. Propagation distance=$7L_D$.

Moreover, Fig. 4 also shows that the $\theta(x,z)$ parameter is conserved in the transverse dimension x at any fixed distance z. This soliton property follows from the relation $\theta(x,z) = \frac{\Delta\varphi(x,z)}{2}$, which can be deduced from Eq. (6a), and from the constancy of the phase difference between the two components of the vector soliton, i.e., $\Delta\varphi(x,z)=\varphi_U(x,z)-\varphi_V(x,z)$ =constant.

As the $s_3(x,z)$ curvature is conserved during propagation, the polarization trajectories can be viewed as a set of arcs of circles on the Poincaré sphere. A linear evolution of the orientation of the polarization ellipse θ is also clearly observable. It corresponds to the rotation of the polarization ellipse due to the nonlinear birefringence, as shown in Fig. 2(b). Finally, Fig. 4 also depicts in dashed line the trajectory of the integrated Stokes parameters and confirms the invariance of S_3 and the rotation of the polarization ellipse. It is important to state that the integrated Stokes parameters plotted in Fig. 4 are not on the surface of the Poincaré sphere but slightly inside, as $S_1^2+S_2^2+S_3^2<S_0^2$. This is the result of loss of coherence of integrated Stokes parameters, as discussed previously.

2. Hyperbolic-secant input beam

If we now assume two hyperbolic-secant transverse input profiles for the two components U and V of the vector soliton but with a uniform ellipticity across the beam, we may expect a nonlinear reshaping of the q parameter during the EPVS generation. Figure 5 illustrates the results of such numerical simulations performed both in the linear and in the soliton regimes for a long propagation distance of $7L_D$.

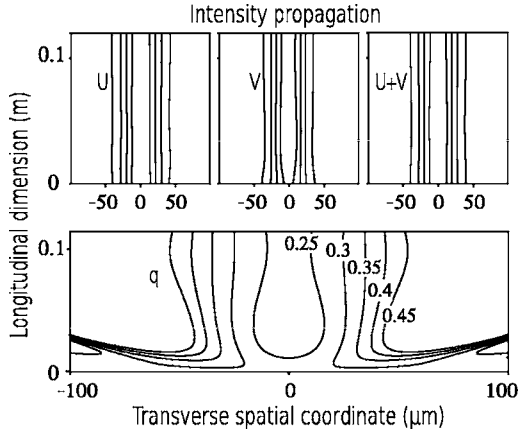

FIG. 6. Contour plot showing the evolution along $7L_D$ of (a) the U component, (b) the V component, (c) the vector soliton, and (d) the ellipticity factor q in the soliton regime.

Figures 5(a) and 5(b) show E_X, E_Y and U,V input hyperbolic transverse intensity profiles (solid and dashed curves), respectively, with the uniform initial q profile (dotted) also shown in (b). Figures 5(c) and 5(d) represent the same profiles after linear propagation. We can see a large amount of diffraction but no polarization change, which is expected since the medium is isotropic. Indeed, the q profile plotted as a dotted line remains flat. On the other hand, Figs. 5(e) and 5(f) depict the situation when the soliton regime is reached. We can clearly observe some energy exchange between the two linear components E_X and E_Y of the vector soliton resulting from polarization rotation, but not between the circular ones. Moreover, the q profile is no more flat and exhibits a curved-shape profile with a dip at the beam center, as expected from the exact EPVS solution [30].

To clearly identify soliton propagation, we then numerically calculated the longitudinal evolution of the U and V components as well as the total field intensity in the soliton regime [see the contour plots in Figs. 6(a)–6(c), respectively]. The nonlinear regime is characterized by the invariant propagation of the total vector soliton. No significant evolution of the most intense component U can be seen in Fig. 6(a), whereas an initial reshaping of V is noticeable in Fig. 6(b). As the V component is slightly less intense than the U component, it is strongly guided and reshaped by XPM with U. Figure 6(d) also illustrates as a contour plot the evolution of the polarization ellipticity factor q in the soliton regime. As the input beam does not correspond to a stable soliton solution, the polarization ellipticity q changes during propagation. This longitudinal evolution is due to spatial reshaping of the U and V components towards the stable solution. Once the polarization ellipticity q has decreased at the center of the spatial soliton, it remains constant all along the propagation. The EPVS is therefore a stable soliton attractor and is self-stabilized.

Figure 7 represents the Stokes parameters evolution during the EPVS generation. The input polarization is characterized by a single point as the input ellipticity is constant across the beam [Fig. 5(b)]. During propagation, two parameters drastically change. First, the ellipticity ε acquires a curvature characterized by a length increase of the arcs of

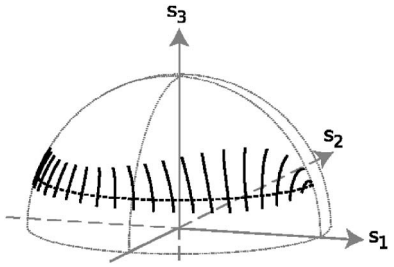

FIG. 7. Polarization evolution of Stokes parameters on the Poincaré sphere for $7L_D$ of propagation for a spatial hyperbolic-secant shaped input beam. The dotted line represents the integrated Stokes parameter.

circles. Second, the ellipse orientation parameter θ increases during the propagation due to the nonlinear birefringence. Additionally, during the initial propagation steps, the arcs of circles exhibit an inflection. This means that the θ angle also depends on the transverse dimension. This behavior is due to the transient reshaping regime of the U and V components before the EPVS generation. As a result, the θ variation is not identical for the top and the wings of the optical beam. When the EPVS is fully generated, however, the arcs of circles tend to be vertical and parallel, meaning that the θ angle is now flat in the transverse direction, as it is the case in Fig. 4. We can conclude from Fig. 7 that there is a transient regime characterized by a change of the ellipticity and of the polarization ellipse orientation. Regarding the evolution of the integrated Stokes parameters (dotted line), its trajectory is similar to the one described in Fig. 4, except that the starting point is on the surface of the Poincaré sphere and ends inside it.

B. Spatiotemporal case: The experimental configuration

To model the experimental conditions as perfectly as possible, both the input spatial and temporal Gaussian profiles of the light pulses must be considered. Here we make the assumption that the spatial evolution is decoupled from the temporal one [38] by considering the pulses used experimentally (600 ps) as quasimonochromatic. This enables us to neglect material or waveguide dispersion. The time dependence of the Kerr nonlinearity is also neglected as the response time in CS_2 (2 ps) is smaller than the pulse duration. With these assumptions, we can use Eqs. (2) with an additional time dimension decoupled from the spatial one. Physically, it is obvious that different temporal slices of the pulse will evolve nonlinearly according to their power. For instance, the trailing and leading edges of the pulse are only affected by diffraction because of their low power. They widen spatially and do not undergo polarization ellipticity change. On the contrary, the pulse peak undergoes self-focusing and a strong polarization evolution. The time-averaged field will therefore be significantly different from what is observed in the continuous-wave regime.

1. Time-integrated spatial profiles

The results of our spatiotemporal numerical simulations are shown in Fig. 8 in the same manner as in Fig. 5 but using

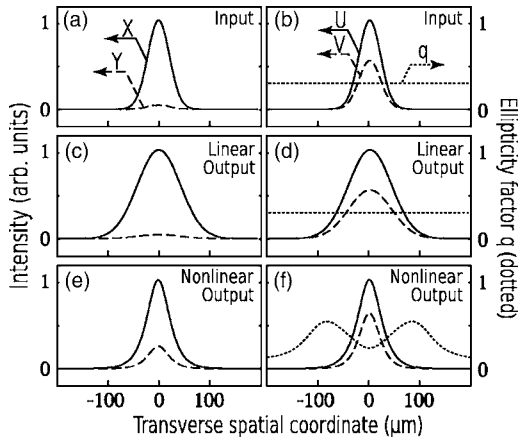

FIG. 8. Numerical results: (a), (c) and (e): E_x (solid line) and E_y (dashed line) intensity profiles for, respectively, the input beam [FWHM=49 μm], the output beam at low power [FWHM =100 μm] and the output beam in the soliton regime [FWHM =49 μm]. (b), (d) and (f): corresponding U (solid line), V (dashed line) and q (dotted line) profiles. Note that in the soliton regime, FWHM(U)=53 μm is different from FWHM(V)=49 μm. Parameters are $k=1.94\times10^7$ m^{-1}, $\gamma=4.1\times10^{-11}$ m.W^{-1}, maximum input intensity $I=4.5\times10^{11}$ W.m^{-2}, propagation distance=3 cm.

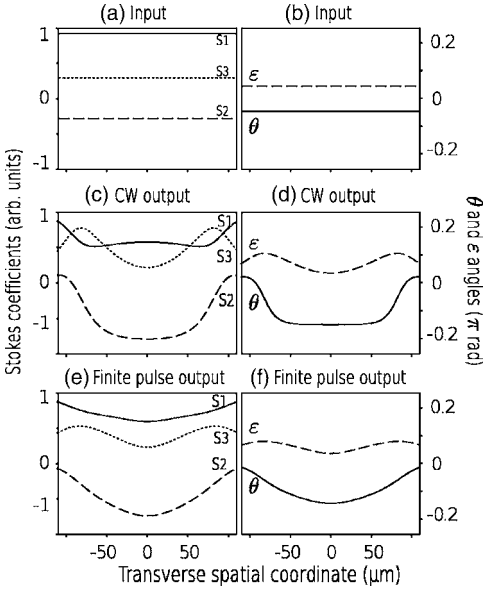

FIG. 9. Transverse polarization parameters of the vector soliton. (a,b) input beam, (c,d) after 3 cm soliton propagation with continuous-wave input, and (e,f) same as (c,d) but for a finite pulse duration.

time-integrated spatial profiles. Here we assume a Gaussian input beam as the initial condition. The propagation distance corresponds to the experimental waveguide length of 3 cm, which is close to $2L_D$. This leads to an output beam in the linear diffraction regime [Figs. 8(c) and 8(d)] which is twice as large as the input one [Figs. 8(a) and 8(b)]. Figures 8(e) and 8(f) show the beam profiles after soliton propagation. The first evidence of vector soliton propagation is the hyperbolic secant reshaping of the two components. Again, the energy exchange between the two linear components E_X and E_Y is clearly observable even though it is reduced in comparison with that observed in Fig. 5 because of the shorter propagation distance. The most noticeable discrepancy, however, is that the gap in the q parameter is not as marked as in the pure spatial case shown in Fig. 5(f). This emphasizes the influence of the pulse wings that can be considered as nonsolitonic radiations (NSR). The q parameter is thus averaged and lowered by the spatiotemporal nature of the laser pulses. The polarization rotation at the center of the beam can be extracted through the ratio between E_x and E_y in Fig. 8: $\Delta\theta^{num}=\theta_{out}-\theta_{in}\approx0.1\pi$.

2. Output Stokes parameters

To get access to the entire polarization state of the beam, we calculated the transverse polarization parameters of the fields using Eqs. (4), (6a), and (6b). Figures 9(a) and 9(b) show, respectively, the normalized Stokes parameters $[s_i(x,0)/s_0,\ i=1,2,3]$ and the corresponding ellipticity angle $\varepsilon(x,0)$ and ellipse orientation angle $\theta(x,0)$, all at the waveguide input face. As can be seen, these parameters drastically change after soliton propagation. Both the results of purely spatial [Figs. 9(c) and 9(d)] and spatiotemporal [Figs. 9(e) and 9(f)] simulations clearly show that every point of the transverse profile has a different polarization. The curvature of ε is directly related to the q factor curvature [see Eqs. (7)] and corresponds to the expected EPVS solution. In addition, the comparison of Figs. 9(d) and 9(f) reveals that the use of a pulsed input beam induces a significant decrease of the amplitude of the ε curve, as previously reported for the q parameter in Fig. 5(f). Note that, for the pure spatial case shown in Fig. 9(d), θ presents a flat profile at the center. This is consistent with the vector soliton properties since the ellipse orientation angle is the same for all points in the transverse spatial dimension. However, this is not the case for the pulsed configuration of Fig. 9(f), for which the θ parameter at a given position x corresponds to the average of the θ values for all the temporal slices of the pulse weighted by their intensity. Therefore this ensemble averaging suppresses the flat θ characteristics of the EPVS.

3. Longitudinal and transverse polarization dynamics

Figure 10(a) illustrates the transverse polarization states for different temporal slices of the vector soliton when the

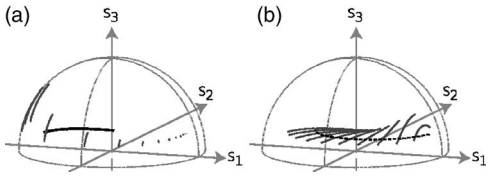

FIG. 10. (a) Evolution of the polarization state of several temporal slices of the spatial EPVS after propagation over $7L_D$. The bold line represents the resulting time-integrated polarization state (this segment is inside the sphere). (b) Corresponding longitudinal polarization evolution of Stokes parameters (these segments progressively sink inside the sphere). The dotted line represents the integrated Stokes parameter evolution (idem).

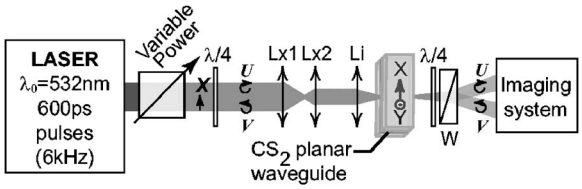

FIG. 11. Experimental setup. $L\times1$, $L\times2$: cylindrical lenses used to shape the soliton in the transverse direction (f_{Lx1} =300 mm, f_{Lx2}=150 mm). Li: injection lens (f_{Li}=80 mm), W: Wollaston biprism.

propagation distance is equal to $7L_D$. The Stokes parameters of the pulse wings correspond to the short segment lines on the right, while the segments on the left correspond to the peak of the pulse. It is clear from this figure that each temporal slice has different ellipticity parameters and a different polarization orientation. The bold line is the time-integration of the previous Stokes parameters weighted by their respective intensities. As can be seen, the segment line is no more vertical but exhibits a strong tilt, due to the change of the θ parameter in the transverse dimension, as previously discussed from Fig. 9(f). Second, as for a partially polarized light, the dispersion of the polarization state of the different temporal parts of the pulse yields an averaged state inside the sphere (bold line), which strongly differs from the previous results which did not take into account the finite pulse duration.

The evolution of the Stokes parameters during the propagation of the spatiotemporal field up to a propagation distance of $7L_D$ is represented in Fig. 10(b). The last segment line then corresponds to the bold line of Fig. 10(a). It is significant that the polarization state evolution during propagation differs from the purely spatial case (Fig. 7) and that the generation of the EPVS does not correspond to vertical arcs of circles anymore.

IV. EXPERIMENT

The experiment, schematically sketched in Fig. 11, is performed in a 3 or 7 cm-long CS_2 liquid planar slab waveguide. The step-index waveguide is made of a 15-μm-thick CS_2 layer sandwiched between two SK5 glass plates, whose index difference is Δn=0.04 [29]. A beat length of L=1.8 m=106L_D much longer than the waveguide length was measured, which ensures a quasi-isotropic condition required to generate and maintain the EPVS. As a pump laser, we used a compact passively Q-switched microchip Nd:YAG laser emitting 600 ps Gaussian pulses at a repetition rate of 6.7 kHz and at a wavelength of 532 nm (mean power is 30 mW). The high power stability (<1% rms) as well as the smooth circular TEM00 beam profile of the laser allow one to generate the spatial soliton with an excellent transverse stability and, therefore to measure accurately its polarization state.

The elliptic polarization state of the input beam was adjusted by means of a quarter-wave plate. A couple of cylindrical lenses ($Lx1$, $Lx2$) are inserted to adjust the horizontal size x of the beam (soliton width) without changing the vertical size y. At the waveguide's output, a second quarter-wave plate and a Wollaston biprism (W) were used to extract either the (E_x,E_y) linearly polarized components or the (U,V) circularly polarized components depending on the wave-plate and prism orientations. First, to get access to the global polarization state, we directly observe the energy ratio between the linearly polarized components. Second, the ellipticity factor across the transverse beam profile is measured by means of the circularly polarized components [see Eq. (7), with time-averaged U, V components].

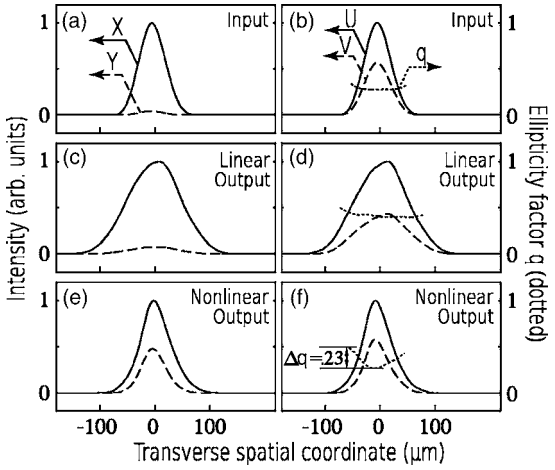

FIG. 12. Experimental results: (a), (c), and (e): E_x (solid line) and E_y (dashed line) intensity profiles of, respectively, the input beam (FWHM=49 μm), the output beam at low power (FWHM =100 μm), and the output beam in soliton regime (FWHM =51 μm). (b), (d), and (f): intensity profiles for left-handed U (solid line) and right-handed V (dashed line) circular polarizations and ellipticity factor q (dotted line). Note that in soliton regime, FWHM(U)=53 μm is different from FWHM(V)=45 μm.

A. Time-integrated spatial profiles

The experimental results are detailed in Fig. 12. Figures 12(a), 12(c), and 12(e) illustrate the E_x and E_y profiles at the waveguide's input and output in linear and soliton regimes, respectively, while Figs. 12(b), 12(d), and 12(f) exhibit the U, V, and q (dotted line) intensity profiles in the same conditions. The first quarter-wave plate is tuned so that the input ellipticity factor is 0.29 and is of course constant all across the transverse beam profile, as shown by the dotted line of Fig. 12(b). This particular value (q=0.29) has been chosen through numerical simulations to get a maximum decrease in the q parameter at the beam center. For this ellipticity degree, one can see in Fig. 12(a) that the power of the E_y polarization is much lower than the E_x one.

Figures 12(c) and 12(d) show the same profiles after linear propagation within the waveguide. We can see clear diffraction of the beam whose FWHM is twofold compared to the input one. The ellipticity profile is still flat across the beam and no polarization rotation occurs. Note that no significant energy exchange between the E_x and E_y components is observable, which confirms the isotropic assumption.

The soliton regime is reached for a mean pump power of 4 mW (maximum intensity of 4.4×10^{11} W m^{-2}) and the

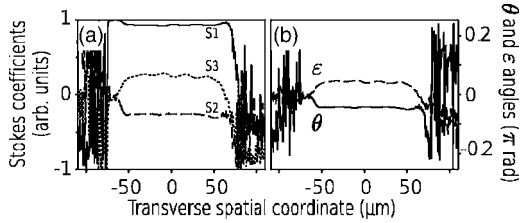

FIG. 13. Experimentally measured transverse polarization parameters in the input beam. (a) Stokes parameters s_1 (solid line), s_2 (long-dashed line), and s_3 (dotted line), normalized by s_0. (b) Ellipticity angle ε (long-dashed line) and ellipse orientation angle θ (solid line).

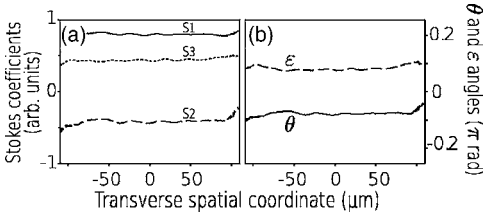

FIG. 14. Experimentally measured transverse polarization parameters in the linear output beam. (a) Stokes parameters s_1 (solid line), s_2 (long-dashed line), and s_3 (dotted line), normalized by s_0. (b) Ellipticity angle ε (long-dashed line) and ellipse orientation angle θ (solid line).

output spatial profiles are presented in Figs. 12(e) and 12(f). They show clear reshaping of the input Gaussian beams into hyperbolic secant-shaped profiles for both linear and circular polarizations. In addition, the E_y polarization shown in Fig. 12(c) has much more energy than in the linear regime, meaning a global polarization rotation of the soliton. Note that in planar waveguide with linear birefringence, this TM component is unstable and leads to the so-called polarization instability [11,37,39]. Figure 12(f) demonstrates that the polarization state is no longer uniform across the entire beam and the ellipticity factor exhibits a difference of $\Delta q=0.23$ between the center and the wings of the beam, as predicted by our numerical simulations. We also measured FWHMs of the U and V beams of 53 and 45 μm, respectively. As a matter of fact, a nonlinear reshaping of the U and V circular polarizations of the beam occurs during propagation without energy exchange between both components, leading to different widths for the U and V beams.

B. Stokes parameters measurements

In order to get access to the entire polarization state of the soliton, we used the setup described in Fig. 11 under different configurations. As explained in Ref. [36], the polarization parameters can be deduced by measuring six intensities obtained by changing the orientation of the quarter-wave plate and the Wollaston biprism. The input polarization is depicted in Fig. 13. We have plotted (a) the Stokes parameters of the input beam and (b) the ellipse angles. We can observe that all polarization parameters are constant, as in Figs. 9(a) and 9(b). Note that the polarization parameters measured outside of the optical beam are strongly noisy because of the very low power.

Figure 14 illustrates the same parameters measured at the output end of the waveguide in the low power regime. We can see that all the transverse polarization parameters remain flat. The values of these parameters are, however, a bit modified. This is also noticeable through the small difference in the q value between Figs. 12(b) and 12(d). This difference could be interpreted as the action of the residual linear birefringence of the waveguide. But the thickness of the waveguide was not narrow enough to explain this phenomenon, and the fact that the parameter s_1 is also modified confirms that the linear birefringence does not come from the waveguide. Actually this small change in the polarization state has been identified as resulting from a low stress-induced birefringence of some optical elements in the setup, and mainly the windows of the CS_2 tank. Thus the assumption of an isotropic propagation in the waveguide is still valuable.

Figures 15(a) and 15(b) display the polarization parameters measured in the nonlinear soliton regime after 3 and 7 cm propagation lengths, respectively. Direct comparison between the experimental data and spatiotemporal numerical simulations taken from Figs. 9(e) and 9(f) shows a fairly good agreement, highlighting the significant impact of finite pulse duration on the vector spatial soliton generation. As expected, the spatial output profiles of these parameters are not flat anymore in comparison to the input ones. This comparison confirms that the temporal finite width of the input beam must be taken into account in order to well understand the experimental polarization measurements. For example, the experimental polarization axis rotation of the top of the beam is $\Delta\theta^{exp}=\theta_{out}-\theta_{in}\approx 0.15\pi$, in quite good agreement with the numerically calculated one.

To complete our experimental investigation, we performed additional measurements of the state of polarization over a longer propagation length of 7 cm, meaning more than $4L_D$. The results are plotted in Fig. 15(b). For such longer propagation, it is significant that we achieved a very good agreement between simulations and experiments. It is

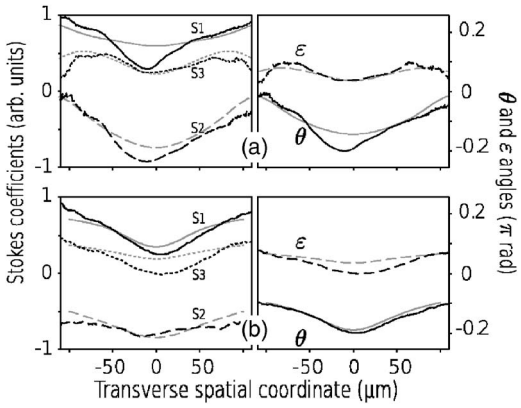

FIG. 15. Experimentally measured transverse polarization parameters of the EPVS after (a) 3 cm and (b) 7 cm propagation. Left column: Stokes parameters s_1 (solid line), s_2 (long-dashed line), and s_3 (dotted line), normalized by s_0. Right column: ellipticity angle ε (long-dashed line) and ellipse orientation angle θ (solid line). In gray are plotted the numerical results of Figs. 9(e) and 9(f).

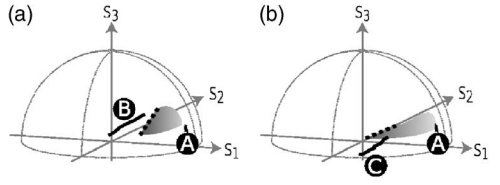

FIG. 16. Polarization dynamics of the vector soliton on the Poincaré sphere for (a) 3 cm and (b) 7 cm, respectively. A: starting point, B: output polarization after 3 cm, and C: after 7 cm. Gray areas and dotted lines are numerical simulations. Solid lines represent experimental measurements. Note that the output states (B,C) are slightly inside the sphere.

important to note that the measurements for 7 cm propagation have been made with a lower input power than for 3 cm, to prevent from stimulated Raman scattering. Consequently, we can measure a lower $\Delta\theta$ for a 7 cm length and this results in a 70 μm wide beam at the waveguide's output.

1. Longitudinal and transverse polarization dynamics

In Figs. 16(a) and 16(b) are projected, on the Poincaré sphere, the polarization dynamics during the EPVS generation for 3 and 7 cm lengths, respectively. The starting point A is also plotted. The corresponding simulated trajectories are shown in gray and the final state is shown by a dotted line. This representation confirms the good qualitative agreement between our experimental measurements depicted in solid lines and the theoretical expectations. We can see both the longitudinal ellipse rotation and the transverse ellipticity curvature of the elliptically polarized fundamental vector soliton. We also observe the transverse ellipse rotation variation only due to the time integration and characterized by a tilt in the line segments.

V. CONCLUSION

In conclusion, we have carried out a complete experimental and numerical characterization of the fundamental elliptically polarized vector soliton of isotropic Kerr media. This was achieved in the spatial domain in a slab planar waveguide with the help of an original polarization-measurement setup. Our observations have revealed its typical polarization evolution, in particular, the continuous ellipse rotation of the vector soliton during propagation and its curved-shape ellipticity profile, which is due to cross-phase modulation between the two circularly polarized components of the soliton. We have additionally demonstrated through spatiotemporal numerical simulations that the finite pulse duration of the optical beam has a significant influence on the observed transverse polarization evolution of the spatial vector soliton, leading to a whole complex polarization dynamics. With this model, we obtained a very good agreement with experimental measurements of the polarization evolution of the vector spatial soliton, showing that the finite pulse duration in spatial soliton generation must be carefully taken into account.

ACKNOWLEDGMENTS

This work was supported by the Ministère délégué à la recherche. The authors thank S. Coen for careful reading.

[1] P. D. Maker, R. W. Terhune, and C. M. Savage, Phys. Rev. Lett. **12**, 507 (1964).
[2] G. Gregori and S. Wabnitz, Phys. Rev. Lett. **56**, 600 (1986).
[3] M. V. Tratnik and J. E. Sipe, Phys. Rev. A **38**, 2011 (1988).
[4] D. N. Christodoulides and R. I. Joseph, Opt. Lett. **13**, 53 (1988).
[5] C. M. De Sterke and J. E. Sipe, Opt. Lett. **16**, 202 (1991).
[6] M. Haelterman and A. P. Sheppard, Phys. Rev. E **49**, 3389 (1994).
[7] S. G. Murdoch, R. Leonhardt, and J. D. Harvey, Opt. Lett. **20**, 866 (1995).
[8] S. F. Feldman, D. A. Weinberger, and H. G. Winful, J. Opt. Soc. Am. B **10**, 1191 (1993).
[9] Y. Chen, Phys. Rev. E **57**, 3542 (1998).
[10] D. C. Hutchings, J. M. Arnold, and D. F. Parker, Phys. Rev. E **58**, 6649 (1998).
[11] R. Malendevich, L. Friedrich, G. I. Stegeman, J. M. Soto-Crespo, N. N. Akhmediev, and J. S. Aitchison, J. Opt. Soc. Am. B **19**, 695 (2002).
[12] Y. Silberberg and Y. Barad, Opt. Lett. **20**, 246 (1995).
[13] S. Trillo, S. Wabnitz, R. H. Stolen, G. Assanto, C. T. Seaton, and G. I. Stegeman, Appl. Phys. Lett. **49**, 1224 (1986).
[14] S. Wabnitz, Phys. Rev. A **38**, 2018 (1988).
[15] J. U. Kang, J. S. Aitchison, G. I. Stegeman, and N. Akhmediev, Opt. Quantum Electron. **30**, 649 (1998).
[16] D. Wang, R. Barillé, and G. Rivoire, J. Opt. Soc. Am. B **15**, 2731 (1998).
[17] V. Boucher, H. Leblond, and X. Nguyen-Phu, Phys. Rev. E **68**, 056604 (2003).
[18] M. N. Islam, C. E. Soccolich, and J. P. Gordon, Opt. Lett. **15**, 21 (1990).
[19] N. Akhmediev and J. M. Soto-Crespo, Phys. Rev. E **49**, 5742 (1994).
[20] J. M. Soto-Crespo, N. Akhmediev, and A. Ankiewicz, J. Opt. Soc. Am. B **12**, 1100 (1995).
[21] C. De Angelis, P. Franco, and M. Romagnoli, Opt. Commun. **157**, 161 (1998).
[22] E. Seve, G. Millot, S. Wabnitz, T. Sylvestre, and H. Maillotte, J. Opt. Soc. Am. B **16**, 1642 (1999).
[23] N. N. Akhmediev, A. V. Buryak, J. M. Soto-Crespo, and D. R. Andersen, J. Opt. Soc. Am. B **12**, 434 (1995).
[24] B. C. Collings, S. T. Cundiff, and N. Akhmediev, J. Opt. Soc. Am. B **17**, 354 (2000).
[25] B. A. Malomed, Phys. Rev. A **43**, 410 (1991).
[26] Y. Barad and Y. Silberberg, Phys. Rev. Lett. **78**, 3290 (1997).
[27] E. A. Ostrovskaya, N. N. Akhmediev, G. I. Stegeman, J. U. Kang, and J. S. Aitchison, J. Opt. Soc. Am. B **14**, 880 (1997).
[28] P. Kockaert, M. Haelterman, S. Pitois, and G. Millot, Appl. Phys. Lett. **75**, 2873 (1999).
[29] C. Cambournac, T. Sylvestre, H. Maillotte, B. Vanderlinden, P.

Kockaert, P. Emplit, and M. Haelterman, Phys. Rev. Lett. **89**, 083901 (2002).
[30] M. Haelterman and A. P. Sheppard, Phys. Lett. A **194**, 191 (1994).
[31] J. U. Kang, G. I. Stegeman, J. S. Aitchison, and N. Akhmediev, Phys. Rev. Lett. **76**, 3699 (1996).
[32] M. Delqué, T. Sylvestre, H. Maillotte, C. Cambournac, P. Kockaert, and M. Haelterman, Opt. Lett. **30**, 3383 (2005).
[33] J. T. Chen, Q. D. Liu, P. P. Ho, and R. R. Alfano, J. Opt. Soc. Am. B **12**, 907 (1995).
[34] C. Cambournac, H. Maillotte, E. Lantz, J. M. Dudley, and M. Chauvet, J. Opt. Soc. Am. B **19**, 574 (2002).
[35] R. W. Boyd, *Nonlinear Optics* (Academic Press, San Diego, 1992).
[36] R. M. A. Azzam and N. M. Bashara, *Ellipsometry and Polarized Light* (Elsevier Science, New York, 1999).
[37] B. Daino, G. Gregori, and S. Wabnitz, Opt. Lett. **11**, 42 (1986).
[38] C. Froehly, B. Colombeau, and M. Wampouille, *Progress In Optics* (Elsevier Science, Amsterdam, 1983), Vol. XX, Chap. 2, p. 78.
[39] H. G. Winful, Opt. Lett. **11**, 33 (1986).